# Optical properties of nanosized particles dispersed in colloidal solutions or arranged in 2D or 3D superlattices

**Marie Paule Pileni**

*Laboratoire SRSI, (CNRS URA 1662), Université P. et M. Curie (Paris VI), BP 52, 4 Place Jussieu, F75231 Paris cédex 05, France and CEA-CEN Saclay, DRECAM-SCM, F91191 Gif-sur-Yvette cédex, France*

In this paper it is demonstrated that colloidal assemblies used as templates are good candidates for controlling the size and shape of nanoparticles. The optical properties of metal nanoparticles dispersed in a colloidal solution differ with size and shape. When these particles are able to self-assemble, they form monolayers in a hexagonal network or crystal with a face-centered cubic arrangement. Such self-organizations induce changes in the optical properties. The size and composition of II–VI semiconductors are controlled independently. Quantum dots are observed. For semiconductor semimagnetic nanocrystals such as $Cd_{1-y}Mn_yS$, the fluorescence due to isolated $Mn^{2+}$ ions is attributed to the aging of the particles and not to a quantum dot effect, as predicted.

Increasingly, chemists are contributing to the synthesis of advanced materials with enhanced or novel properties by using colloidal assemblies as templates. The fabrication of assemblies of perfect nanometer-scale crystallites (quantum crystals), identically replicated in unlimited quantities in such a state that they can be manipulated and understood as pure macromolecular substances, is the ultimate challenge in modern materials research with outstanding fundamental and potential technological consequences. These potentialities are mainly due to the unusual dependence of the electronic properties on the particle size, either for metal[1–7] or semiconductor[1,2,8–17] particles, in the 1 to 10 nm range.

The preparation and characterization of these nanomaterials have thus motivated a vast amount of work.[18] One of the methods used to control size and/or polydispersity of the particle is the synthesis in reverse micelles.[1,2] We present data that demonstrate that colloidal assemblies are good candidates for controlling the size and shape of nanoparticles and for following their optical properties. When these particles are able to self-assemble, they form monolayers in a hexagonal network or crystal with an fcc structure. The self-organization induces changes in the optical properties.

The use of reverse micelles as microreactors permits the size and composition of II–VI semiconductors to be controlled independently. As an example the optical properties of $Cd_{1-y}Mn_yS$ nanocrystals are presented. It is demonstrated that the fluorescence due to isolated $Mn^{2+}$ is due to the aging of particles and not due to a quantum size effect.

## Theory of Optical Properties of Colloidal Metallic Particles

Optical properties of colloidal particles have been intensively investigated, particularly their dependence on size.[5,19–26] Absorption spectra of colloidal dispersions of metals exhibit broad peaks in the UV/VIS range due to the excitation of plasma resonances or interband transitions and characterize the metallic properties of the material. The UV/VIS absorption spectrum of a fairly dilute dispersion of colloidal particles can be calculated from Mie theory.[27] For small spherical particles (diameter $<20$ nm), the absorption spectrum depends only on the contribution of the dipole term in the Mie summation.[28] Thus, the absorbance, $A$, for a dispersion of $N$ particles per unit volume, can be calculated[29–32] from

$$A = CN\ell/2.303 \quad (1)$$

where $C$ and $\ell$ are the absorption cross section and the optical pathlength, respectively.

### Spherical particles

If the particle dimensions are smaller than the mean free path of the conduction electrons, collisions of these electrons with the particle surface take place. This lowers the effective mean free path. In the limit of $2\pi R < \lambda$, (where $R$ is the radius of the particles and $\lambda$ the wavelength of light in the media), only the electric dipole term, developed in Mie's theory, is significant. Then, the cross section can be expressed as:

$$C = [18\pi V\varepsilon_2(\omega)\varepsilon_m^{3/2}]/\lambda[(\varepsilon_1(\omega) + 2\varepsilon_m)^2 + \varepsilon_2(\omega)^2] \quad (2)$$

where $V$ and $\lambda$ are, respectively, the volume of the spherical particle and the incident wavelength (which corresponds to a frequency $\omega$). The complex relative permittivity of the metal is $\varepsilon(\omega) = \varepsilon_1(\omega) + i\varepsilon_2(\omega)$. For these free-electron metals, $\varepsilon_2(\omega)$ is fairly constant in the UV/VIS range and as is well-known, a maximum in the absorption thus occurs when $\varepsilon_1(\omega) = -2\varepsilon_m$, due to the dipole plasma resonance of the spheres. The wavelength of this plasma resonance is therefore given by the wavelength dependence of $\varepsilon_1(\omega)$. The width and height of the resonance is determined by the $\varepsilon_2(\omega)$ value at its wavelength. There are also peaks or inflections in the absorption spectra of particles of some of the less free-electron metals such as copper, though these features are less prominent than for the free-electron metals. For the former metals, $\varepsilon_2(\omega)$ as well as $\varepsilon_1(\omega)$ vary markedly with wavelength over the UV/VIS range, showing that for these metals some interband excitation accompanies the excitation of the plasma resonance. A consequence of the variation of $\varepsilon_2(\omega)$ as well as $\varepsilon_1(\omega)$ with wavelength is that the peaks or inflections do not lie exactly at the wavelength at which $\varepsilon_1 = -2\varepsilon_m$. For metals, such as silver, that show essentially free-electron behavior in the visible range, $\varepsilon_2(\varepsilon)$ is small and there is a sharp and high absorption peak close to the wavelength at which $\varepsilon_1 = -2\varepsilon_m$, as already noted. Clearly, not only the value of $\varepsilon_2(\omega)$ when $\varepsilon_1 = -2\varepsilon_m$ but also the rate of the change of $\varepsilon_1(\omega)$ with wavelength deter-

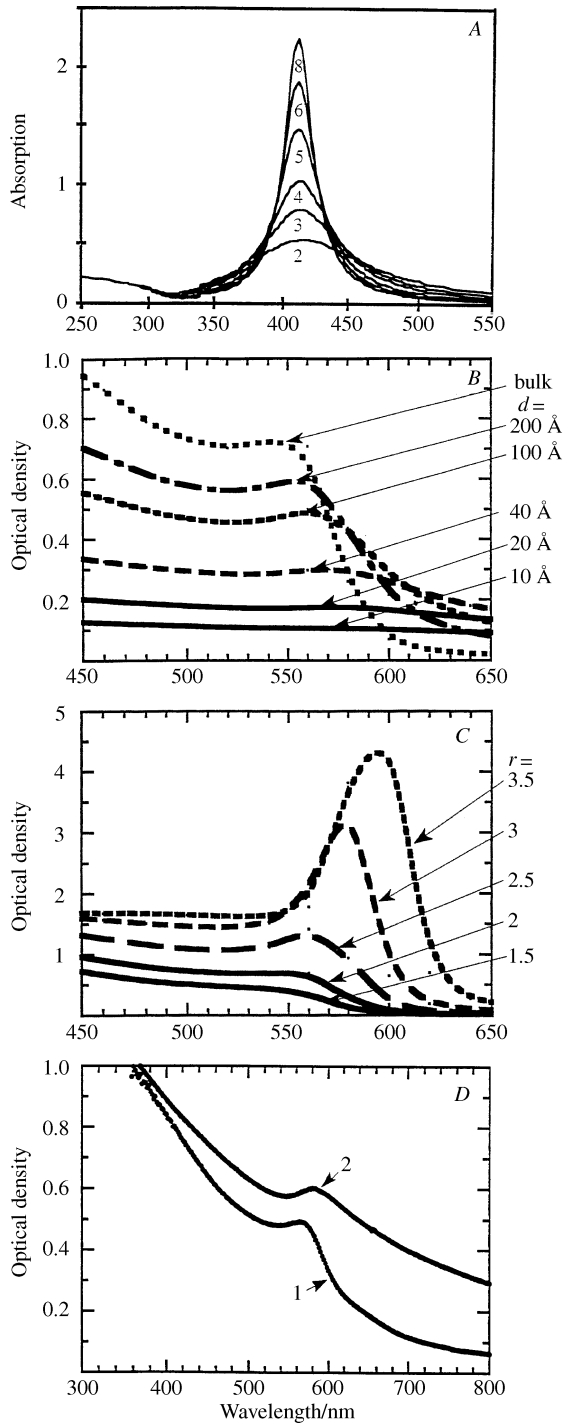


**Fig. 1** Simulation of the absorption spectra of colloidal metal particles: (*A*) spherical silver metal particles with size (in nm); (*B*) spherical copper metal particles with diameter; (*C*) cylindrical copper metal particles with ratio *r*, the minor diameter is equal to 100 Å; (*D*) copper metal particles surrounded by copper oxide layer(s)

mine the spectral width of the absorption band. This depends also on the surrounding medium.

If the particle sizes are comparable with the mean free path of the conduction electrons, *L*, then collisions of the conduction electrons with the particle surfaces become appreciable and thus the effective mean free path is less than that in bulk material. The electron energy bands are quantized and the number of discrete energy levels is the order of magnitude of the number of atoms in the crystal. If the particles contain only around one hundred atoms, the intensities between these levels of the conduction band of the metal particles are no longer smeared out thermally. The intraband transitions of the conduction electrons are thus influenced and this leads to a damping of electron motion, which corresponds to the free path effect in the classical approach. This damping affects the dielectric constant. A second term, $\varepsilon_{2Q}(\omega)$, in the imaginary dielectric permittivity, $\varepsilon_2(\omega)$, must be added if the particles are small:[20]

$$\varepsilon_{2Q}(\omega) = \varepsilon_2(\omega) + \varepsilon_{2S}(\omega) \quad (3)$$

where $\varepsilon_{2S} = L/R$ is the surface contribution due to the small size of the particle.

By using this value of $\varepsilon_{2Q}(\omega)$ instead of $\varepsilon_2(\omega)$, the size effect on the optical constant is taken into account. This modified optical constant is then used in the Mie equations to calculate colloidal absorption bands and involves a broadening and a decrease in the height of the plasmon absorption bands.[5,19–26] The absorption spectra of colloidal particles with different sizes are simulated from eq. (1) and (2) and these simulated spectra for $(Ag)_n$ and $(Cu)_n$ nanosized particles with different sizes are shown in Fig. 1*A* and 1*B*, respectively.

### Prolate spheroidal particles

It is well-known that the absorption spectra of small particles such as copper depend markedly on the particle shape.[33–36]

The mean absorption cross-section for a prolate spheroidal particle, averaged over all orientations, is calculated in the dipole approximation by:

$$C = (8\pi^2/3\lambda)\mathrm{Im}(\alpha_l + 2\alpha_t) \quad (4)$$

where $\alpha_l$ and $\alpha_t$ are, respectively, the polarizabilities of the spheroid along the longitudinal and transverse axes. These are given by:

$$\alpha_{l,t} = V(\varepsilon - 1)/[4\pi + (\varepsilon - 1)P_{l,t}] \quad (5)$$

in which $V$ and $\varepsilon$ are, respectively, the volume of the spheroid whose axial ratio is $r$ ($r > 1$) and the complex relative permittivity of the metal, while $P_{l,t}$, the dipolar moments of the spheroid along the longitudinal and transverse axes, are given by:

$$P_l = [4\pi/(1 - r^2)] \times \{[r/(r-1)^{1/2}]\mathrm{Ln}[r - (r^2 - 1)^{1/2}] + 1\} \quad (6a)$$

$$P_t = (4\pi - P_l)/2 \quad (6b)$$

The absorption spectra for the various ratios ($1.5 \leqslant r \leqslant 3.5$) of the copper particles are simulated for a minor diameter of 10 nm (Fig. 1*C*). It can be observed that for high aspect ratio copper spheroids, the transverse dipole resonance is damped and becomes insignificant compared to the longitudinal resonance. In addition, on elongating the metal particles, we observe a substantial shift of the longitudinal resonance to longer wavelengths, which increases with wavelength.

## Colloidal Self-assemblies used as Templates

To synthesize colloidal metal dispersions, several self-assemblies have been used as templates.[1,2] This has mainly involved reverse micelles, however, normal micelles can be used to make nanosized particles. The nanoparticles are dispersed in an optically clear colloidal solution. This allows the dependence of the metal particle optical properties on their size to be observed.

Reverse micelles are well-known to be spherical water-in-oil droplets stabilized by a monolayer of surfactant. The phase diagram of the surfactant sodium bis(2-ethylhexyl)sulfosuccinate, called Na(AOT), with water and isooctane shows a very large domain of water-in-oil droplets and due to this it is the surfactant most often used to form reverse micelles.[1,2,37] The water pool diameter is related to the water content, $w = [H_2O]/[AOT]$, of the droplet by $D(\mathrm{nm}) = 0.3w$. From the

existing domain of water-in-oil droplets in the phase diagram, the droplet diameters vary from 0.5 nm to 18 nm.

Reverse micelles are dynamic[37–41] and attractive interactions between droplets take place. The intermicellar potential decreases either by decreasing the number of carbon atoms of the bulk solvent or by increasing the number of droplets. This is due to the discrete nature of solvent molecules and is attributed to the appearance of depletion forces between two micelles (the solvent is driven off between the two droplets).[40] When the droplets are in contact, forming a dimer, they exchange their water contents. This exchange process is associated with the interface rigidity, which corresponds to the bending elastic modulus of the interface.[41] Hence, in collisions the droplets exchange their water contents and again form two independent droplets. This process has been used to make metal nanosized particles by chemical reduction of metallic ions.[1–7] We demonstrate below that these various factors (water content, intermicellar potential) control the particle size.

Surfactants having a positive curvature, above a given concentration usually called the critical micellar concentration, cmc, self-assemble to form oil-in-water aggregates called normal micelles. The most often used surfactant is sodium dodecylsulfate, Na(DS). To make particles, the counter ion of the surfactant is replaced by ions that participate in the chemical reaction. These are called functionalized surfactants. Hence, to make copper metal particles, copper dodecylsulfate, $Cu(DS)_2$, is used. It is made by mixing an aqueous solution of sodium dodecylsulfate with copper sulfate, as described elsewhere.[42] Concentrations of 0.1 M of these two solutions are employed and the mixture kept at 2 °C. The resulting precipitate is washed several times with the 0.1 M copper sulfate solution and recrystallized in distilled water. $Cu(DS)_2$ forms micellar aggregates above the cmc of $1.2 \times 10^{-3}$ M. The shape and the size of these aggregates have been determined by SAXS and by light scattering. They were found to be prolate ellipsoidal micelles with a hydrodynamic radius of 2.7 nm and having sizes and shapes similar to those observed with the cadmium derivative.[43]

## Syntheses and Optical Properties

### Spherical nanoparticles of different sizes

**Silver nanosized particles.** Colloidal silver particles are prepared by mixing two reverse micellar solutions at the same water content. One contains 30% Ag(AOT), 70% Na(AOT) and the other Na(AOT) and sodium tetraborohydrate, $NaBH_4$. This induces formation of silver particles, $(Ag^0)_n$,[4] which takes place within a few minutes in the presence of air. The particle size depends on the droplet diameter, that is, on the water content. The absorption spectra of colloidal silver particles obtained in micelles at various water contents, *w*, are shown in Fig. 2. These spectra are characteristic of silver metal particles with a plasmon absorption band centered at 400 nm. At low water content, the absorption spectrum is broad with a low optical density. On increasing the water content, the plasmon peak is narrower, more intense and slightly blue-shifted. On the other hand, the absorbance at 250 nm increases slightly with the water content. Comparison of Fig. 1*A* and 2 shows an increase in the size of silver particles with the diameter of the spherical template, which is confirmed by TEM patterns (Fig. 3). From the histograms it can be observed that the decrease in the diameter of reverse micelles induces formation of smaller silver particles, having a lower size distribution. Similar data have been obtained for other inorganic particles and have been attributed to a protective effect of the surfactant.[12] High resolution electron microscopy reveals a crystalline structure with a lattice spacing of 4.08 Å as for fcc bulk silver metal (4.0862 Å). The invariance of the lattice spacing with particle size confirms the appearance of metal properties for small silver particle sizes. A blue-shift of the absorption spectrum maximum is correlated with the size of the crystallites determined from TEM patterns.

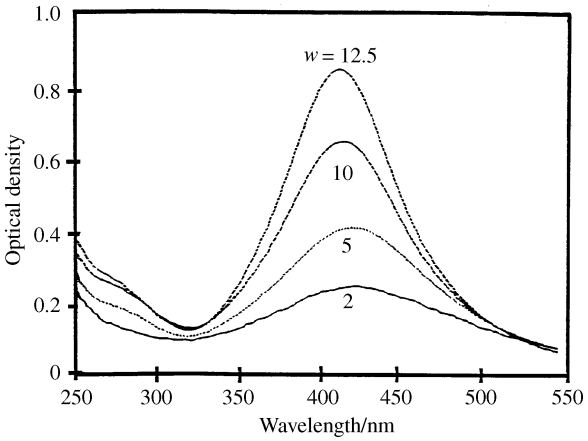


**Fig. 2** Absorption spectra of silver particles formed in [30% Ag(AOT)–70% Na(AOT)]–water–isooctane reverse micelles at various water contents *w*. $[NaBH_4] = 10^{-4}$ M; $[Ag(AOT)] = 1.5 \times 10^{-2}$ M; $[Na(AOT)] = 3.5 \times 10^{-2}$ M; optical path length = 1 mm

As mentioned above, the intermicellar exchange process is governed by the attractive interactions between droplets. The bulk solvent controls the intermicellar potential and consequently the intermicellar rate constant changes by a factor of 10 when replacing isooctane by cyclohexane,[13] whereas the droplet size remains unchanged. Hence, replacing isooctane by cyclohexane and keeping the same experimental conditions $\{w = 7.5$, $[Ag(AOT)] = 3 \times 10^{-2}$ M, $[Na(AOT)] = 7 \times 10^{-2}$

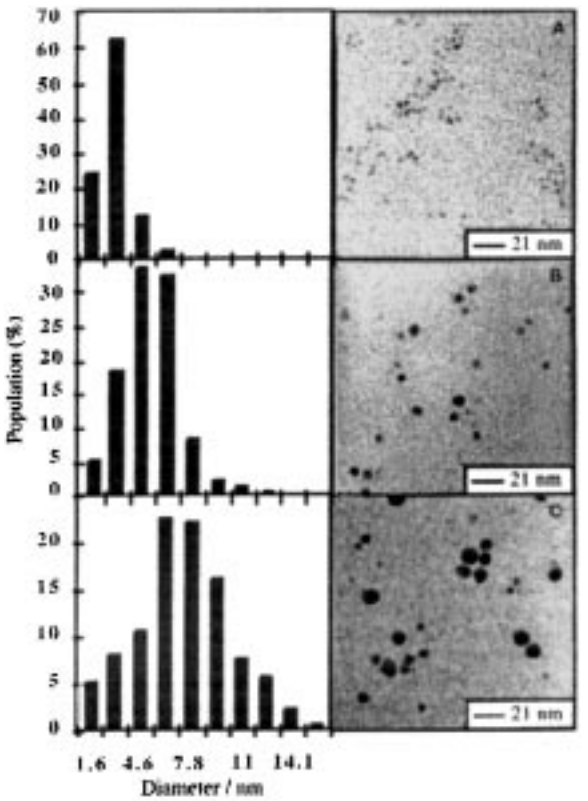


**Fig. 3** Electron micrographs and size distributions of silver crystallites synthesized in Ag(AOT)–Na(AOT)–water–isooctane reverse micelles at various water contents *w*. $[Ag(AOT)] = 3 \times 10^{-2}$ M, $[Na(AOT)] = 7 \times 10^{-2}$ M, $[NaBH_4] = 2.5 \times 10^{-4}$ M. The bars represent 21 nm

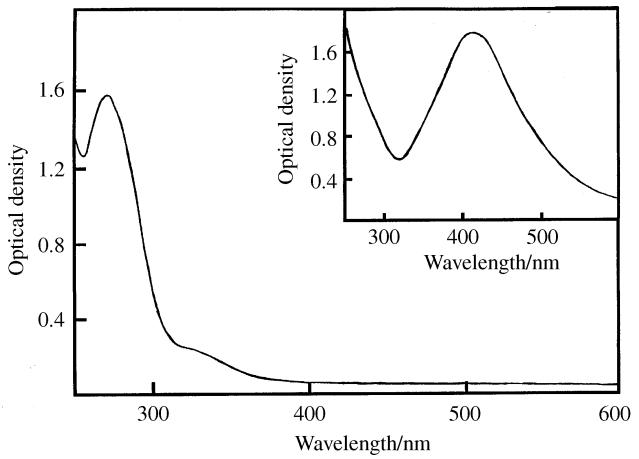


**Fig. 4** Absorption spectrum of $Ag_4^{2+}$ from the reduction of $3 \times 10^{-2}$ M Ag(AOT)–$7 \times 10^{-2}$ M Na(AOT)–cyclohexane. Insert: absorption spectrum of 3.3 nm $(Ag)_n$ particles from the reduction of $3 \times 10^{-2}$ M Ag(AOT)–$7 \times 10^{-2}$ M Na(AOT)–isooctane. The water content is fixed at 7.5, $[NaBH_4] = 10^{-4}$ M. These spectra are obtained when the syntheses are performed in the presence of air

M, $[NaBH_4] = 2.5 \times 10^{-4}$ M} induces a marked change in the observed absorption spectrum, immediately after addition of the reducing agent (Fig. 4). This spectrum is characterized by a maximum centered at 275 nm, attributed to $Ag_4^{2+}$ clusters.[44,45] With time, the size of the clusters increases to reach particles having an average diameter of 3.3 nm (insert Fig. 4). Hence, $Ag_4^{2+}$ is stable for several hours in reverse micelles. Usually, such clusters are characterized by short lives[44,45] at room temperature, except when they are formed in glass or in silver films by reduction under surfactant monolayers.[46]

Due to the strong affinity of the SH headgroup for the noble metal,[47] there is a selective reaction of dodecanethiol with the silver particles. The attachment of dodecanethiol to the silver particles can be monitored by UV/VIS spectroscopy; as shown in Fig. 5 (dotted line) there is a drastic decrease in the extinction coefficient of the plasmon band after dodecanethiol addition, whereas below 300 nm, no change in the UV absorption is observed. This large decrease in the intensity and the red-shift of the maximum observed in the absorption spectrum for coated particles are due to a change in the free electron density. This induces changes in the surface plasmon band of silver particles[26] and produces a variation in the width and maximum of the plasmon band absorption.[26,48] Similar behavior has been observed by NaSH addition to silver colloids in aqueous solution.[49]

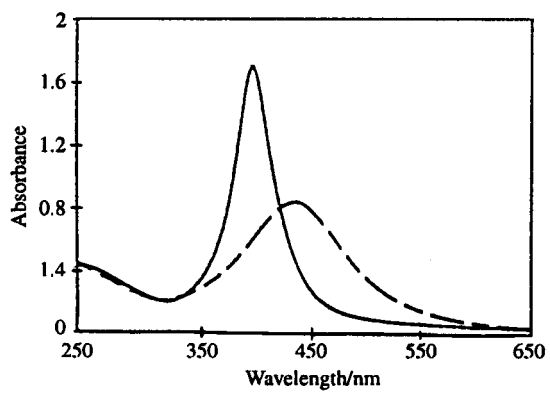


**Fig. 5** UV/VIS absorption spectra of silver colloidal solutions after synthesis in reverse micelles (——) and after addition of dodecanethiol to the micellar solution (– – –)

**Control of the size of copper nanomaterials.** It is well-known that copper can be oxidized though in the bulk phase, the surface is passivated. Copper nanosized particles are characterized by a plasmon peak (Fig. 1*B*). When copper particles are surrounded by oxide layers, the plasmon peak remains centered at 566 nm while a residual absorption characteristic of copper oxide at 800 nm is also observed[50] (Fig. 1*D*). Copper oxide formation can thus be determined by the appearance of an absorption at 800 nm and by electron diffraction patterns. In solution, the copper nanosized particles are usually unstable with immediate formation of the oxide. Reverse micelles are good candidates for forming nanosized copper particles[3,6,7] and for this a functionalized surfactant such as copper bis(2-ethylhexyl)sulfosuccinate, $Cu(AOT)_2$, is needed. When $Cu(AOT)_2$ is replaced by copper sulfate ($Cu^{2+}$), copper oxide particles are formed instead of the pure metal and, in addition, a few minutes after initiating the reaction, the particles flocculate.

The syntheses are carried out as described above except that Ag(AOT) and $NaBH_4$ are replaced by $Cu(AOT)_2$ and hydrazine, $N_2H_4$, respectively. Copper bis(2-ethylhexyl)sulfosuccinate is reduced and copper particles are formed. They are characterized by TEM, electron diffraction and absorption spectroscopy. The absorption spectra of the colloidal particles and electronic microscopy patterns observed at various $w$ values are shown in Fig. 6. At low water content, there is a continuous absorption spectrum with a shoulder at 570 nm. On increasing the water content, the 570 nm band progressively appears. The electron microscopy pictures show an increase in the size of the particles from 2 to 12 nm on increasing the water content from 1 to 10. At water contents above 10, the size of the particles remains unchanged and the poly-

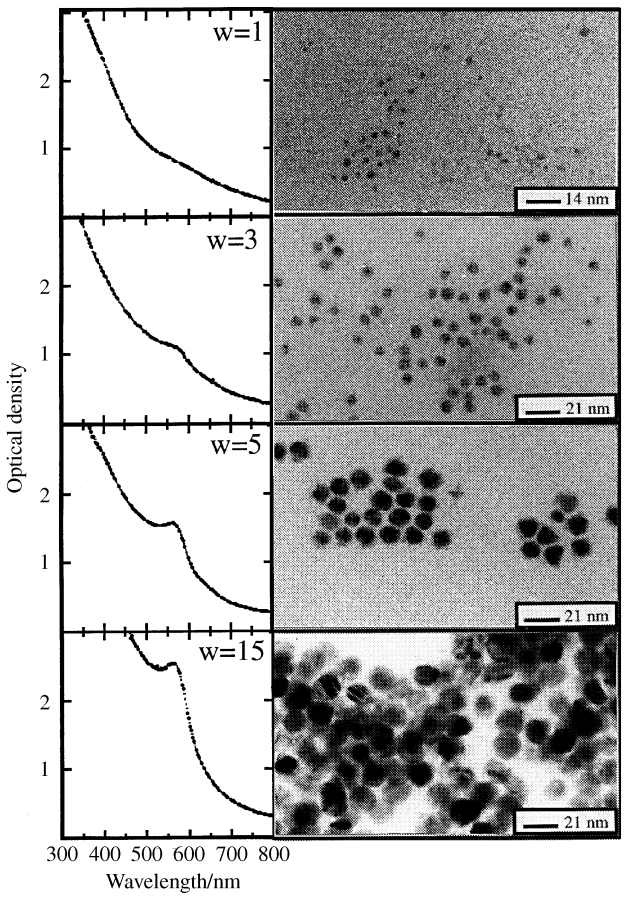


**Fig. 6** Absorption spectra and TEM patterns of copper metal particles synthesized in $Cu(AOT)_2$–Na(AOT)–water–isooctane reverse micelles at various water contents $w$. [AOT] = 0.1 M, $[Cu(AOT)_2] = 10^{-2}$ M, $[N_2H_4] = 3 \times 10^{-2}$ M

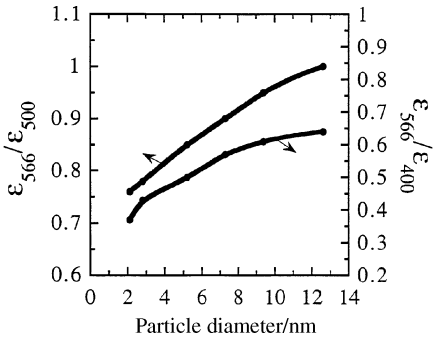


**Fig. 7** Size variation of the extinction coefficient ratios $\varepsilon_{566}/\varepsilon_{500}$ and $\varepsilon_{566}/\varepsilon_{400}$ of the copper particles in a colloidal copper solution, synthesized in $Cu(AOT)_2$–Na(AOT)–water–isooctane reverse micelles: [AOT] = 0.1 M, $[Cu(AOT)_2] = 10^{-2}$ M, $[N_2H_4] = 3 \times 10^{-2}$ M

dispersity increases. Similar behavior of the simulated and experimental absorption spectra in Fig. 1*B* and 6 confirms that the plasmon peak can only be observed with relatively large particles. From the absorption spectra and the electron microscopy patterns given in Fig. 6, it is possible to relate the ratio of extinction coefficients in the cluster absorption spectrum to their size. In fact, each sample is characterized by both UV/VIS spectroscopy and by TEM, which directly gives the distribution of the particle diameters. Then, for each sample, we relate the particle diameter to two absorbance ratios, ($\varepsilon_{566}/\varepsilon_{500}$ and $\varepsilon_{566}/\varepsilon_{400}$) (Fig. 7) and generate a calibration curve from which the particle diameter (the diameter corresponds to the highest frequency on the histograms) can be directly determined from either $\varepsilon_{566}/\varepsilon_{500}$ or $\varepsilon_{566}/\varepsilon_{400}$, as shown in Fig. 7. Therefore, the size of the particles in the 2 to 12 nm range can be derived from electron microscopy or absorption spectroscopy.

As mentioned above, the intermicellar exchange process is governed by the intermicellar potential between droplets and the interface rigidity.[41] The first factor can be modified either by changing the bulk solvent and keeping the same droplet size or by increasing the number of droplets. These two processes have little effect on the interface rigidity. This implies that the intermicellar exchange process is markedly changed either by changing the bulk solvent or increasing the number of droplets. By replacing isooctane with cyclohexane as the bulk solvent, the intermicellar exchange rate constant drops by a factor of 10,[13] inducing a decrease in the particle size (Fig. 8). From these data we conclude that the particle size is not only controlled by the size of the micellar droplet but also by the bulk phase of the colloidal assembly. By keeping the same size of droplets, syntheses are performed at various polar volume fractions, that is at various droplet numbers. Fig. 9 shows a decrease in the particle size with increasing polar volume fraction. Hence, for a given droplet size, the

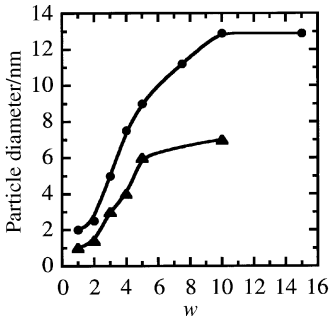


**Fig. 8** Variation of the diameter of copper particles synthesized in $Cu(AOT)_2$–Na(AOT)–water–solvent reverse micelles at various water contents $w = [H_2O]/[AOT]$. [AOT] = 0.1 M, $[Cu(AOT)_2] = 10^{-2}$ M, $[N_2H_4] = 3 \times 10^{-2}$ M. The solvents are (●) isooctane and (▲) cylohexane

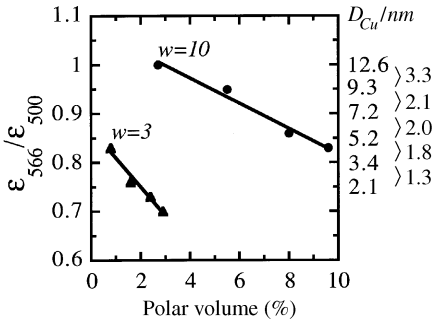


**Fig. 9** Variation of $\varepsilon_{566}/\varepsilon_{500}$ and thus the copper metal particle size with polar volume fraction for two values of *w*

decrease in the intermicellar potential induces a decrease in the average particle size.

### Copper metal nanomaterials of different shapes

Copper(II) dodecylsulfate is reduced by sodium borohydride, $NaBH_4$, using a $NaBH_4 : Cu(DS)_2$ ratio of 2. For all the experimental conditions described below, copper metal aggregates are formed. The syntheses are performed at various $Cu(DS)_2$ concentrations.[51] (*i*) At the critical micellar concentration ($1.2 \times 10^{-3}$ M), the absorption spectrum obtained after chemical reduction is centered at 570 nm (Fig. 10A) with no residual absorption at 800 nm, confirming formation of pure metal particles. A drop of this solution is deposited on a carbon grid and TEM measurements show formation of large domains of aggregates arranged in an interconnected network (Fig. 11A). Enlargement of this image shows an interconnected network corresponding to a change in the metal particle shape and not to aggregation of strongly interacting small particles, (Fig. 11B). (*ii*) Synthesis at $2 \times 10^{-3}$ M $Cu(DS)_2$ induces formation of elongated particles. The absorption spectrum is characterized by a maximum centered at 564 nm (Fig. 10B).

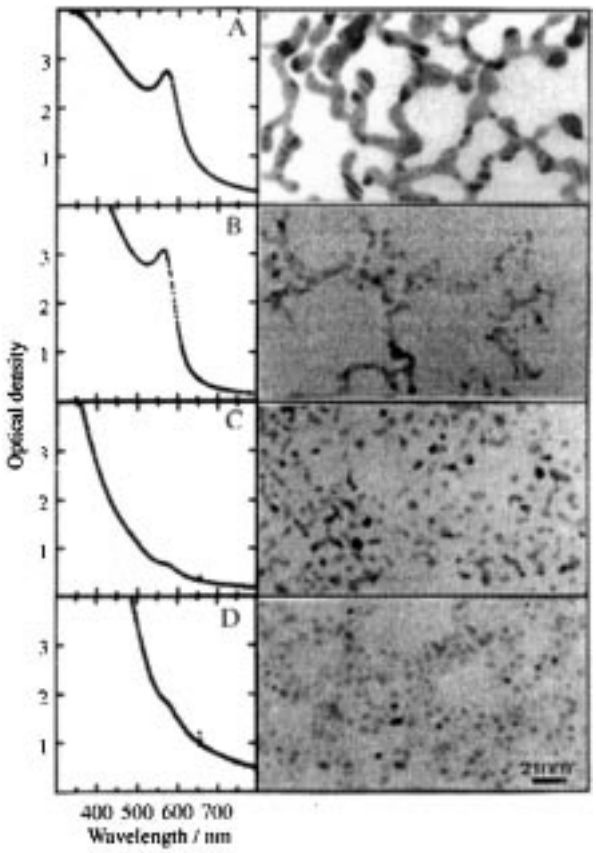


**Fig. 10** Absorption spectra and TEM patterns of colloidal copper dispersions. $[Cu(DS)_2]$ values are: (A) $1.2 \times 10^{-3}$ M, (B) $2 \times 10^{-3}$ M, (C) $3 \times 10^{-3}$ M and (D) $10^{-2}$ M

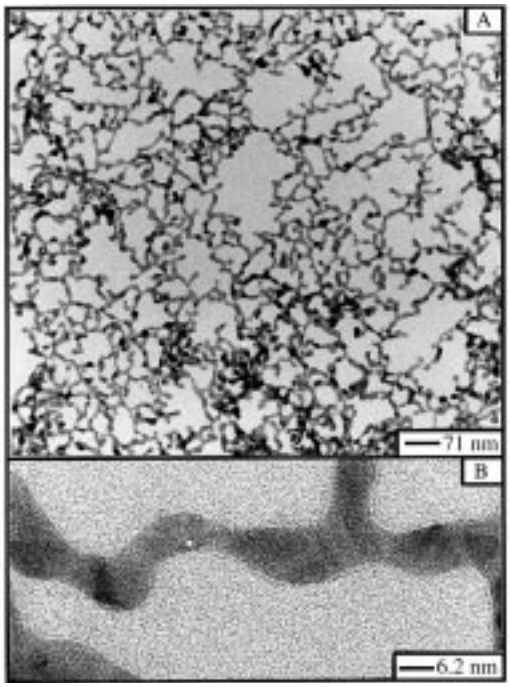


**Fig. 11** TEM micrographs of the copper network prepared in a pure copper dodecylsulfate solution: $[Cu(DS)_2] = 1.2 \times 10^{-3}$ M, $[NaBH_4] = 2.4 \times 10^{-3}$ M, at different magnifications

(*iii*) At higher $Cu(DS)_2$ concentrations, the size of the rods decreases with formation of more spherical particles, (Fig. 10C and D).

Comparison of the absorption spectra for 10 nm diameter spherical particles and other shapes shows a red-shift in the plasmon peak as the shape of the copper particles changes from spheres to rods (Fig. 12). Such changes in the absorption spectra of copper metal particles can be related to those predicted at various $r$ values, where $r$ is defined as the ratio of the length to the diameter of a cylinder.[33–35] The plasmon peak due to the rod particles is centered at 570 nm (Fig. 12). According to simulated absorption spectra,[50] this corresponds to an $r$ value equal to 2.5. From the image analysis of the skeleton of the interconnected network (Fig. 10B), corresponding to a plasmon peak centered at 570 nm, the average length of the linear strands is 22 nm. The average minor diameter is 6.5 nm and thus the $r$ value is to 3.3. From the theoretical predictions such an $r$ value ($r = 3.5$) corresponds to a higher shift in the plasmon peak (620 nm) than that obtained (570 nm). This difference between $r$ and the plasmon peak maximum is explained by the fact that the simulation is related to one size of cylindrical particles. In the present experiment, the particles are interconnected and not isolated cylinders. Furthermore, the size and shape distribution has to

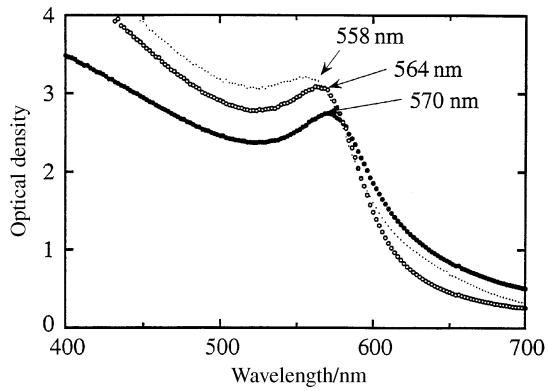


**Fig. 12** Absorption spectra of interconnected (●●●), elongated (○○○) and spherical (···) colloidal particles

be taken into account. A qualitative shift in the maximum of the plasmon peak with the particle shape is in good agreement with those predicted. Hence, the shift and the increase in the absorption band, compared to spherical and elongated particles, indicate that the interconnected network, observed by TEM, exists in solution. It is due to a change in the effective mean free path of the conduction electrons and not caused by the evaporation process of the solutions.

### Monolayers and fcc crystals made of silver spherical nanoparticles

$(Ag)_n$ particles coated by dodecanethiol are extracted from micellar solution and redispersed in heptane.[52] The size distribution is rather large and reduced through the size-selected precipitation (SSP) technique. The optical spectrum of the coated nanosized particles deposited on a graphite support is recorded in the reflectivity mode and is compared with the spectrum corresponding to free particles in hexane. The optical spectra are normalized to unity.[53]

A drop of a dilute solution of 4.5 nm coated particles in hexane $\{[(Ag)_n] = 2 \times 10^{-5}$ M$\}$ is deposited on a graphite surface. Fig. 13A shows a large area of close-packed nanoparticles organized in a hexagonal network. When the particles are organized in a 2D superlattice, the plasmon peak is shifted toward lower energy than that obtained in solution (Fig. 13B). The coverage support is washed with hexane and the nanoparticles are redispersed in the solvent. The absorption spectrum of the latter solution is similar to that used to cover the support (free particles in hexane). This clearly indicates that the shift in the absorption spectrum of nanosized silver particles is due to their self-organization on the support. The bandwidth of the plasmon peak (1.3 eV) obtained after deposition is larger than that in solution (0.9 eV). This can be attributed to a change in the dielectric constant of the surrounding medium, as has been previously demonstrated by a simulation.[34] Such an increase in the dielectric constant can be attributed to an increase in the silver molecular orbital interactions between particles (dipole coupling), which is due to the close proximity of the metal particles.

By leaving the carbon grid inside the solution and letting

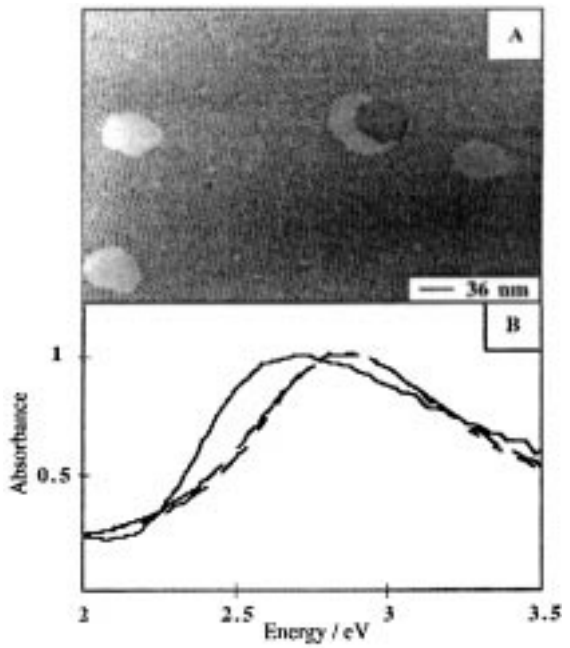


**Fig. 13** Silver nanoparticles of 4.5 nm average diameter. (A) TEM micrograph of the particles organized in a monolayer network on a carbon support. (B) Absorption spectra of $(Ag)_n$ nanoparticles dispersed in solution (– – –) or arranged in a 2D superlattice (——)

the solvent completely evaporate, large aggregates are formed. A rather high aggregate orientation around a large hole or ring is shown in Fig. 14A. The average distance between the oriented aggregates varies from 20 to 60 nm and magnification of these aggregates confirms that they consist of $(Ag)_n$ nanoparticles. Further magnification of one of these aggregates shows that the particles are arranged in two different symmetries. The formation of a polycrystal is shown in Fig. 14B and its magnification (Fig. 14C), shows either a hexagonal or a cubic arrangement of nanoparticles. The transition from one structure to another is abrupt and there is a marked analogy with 'atomic' polycrystals with small grains called nanocrystals. Each domain or grain has a different orientation, clearly showing that the stacking of nanoparticles is periodic and not random. The 'pseudo-hexagonal' structure corresponds to the stacking of a {110} plane of the fcc structure. A fourfold symmetry, which is again characteristic of the stacking of {001} planes of the cubic structure, is observed in the same pattern (Fig. 14C). This cannot be found in the hexagonal structure. As a matter of fact, there is no direction in a perfect hexagonal compact structure for which the projected positions of the particles can take this configuration. This is confirmed by TEM experiments performed at various tilt angles, where it is always possible to find an orientation for which the stacking appears to be periodic. Hence, by tilting a sample having a pseudo-hexagonal structure, a fourfold symmetry is obtained. From these results, it is concluded that the large aggregates of silver particles are formed by stacking of monolayers in an fcc arrangement.

By increasing the concentration of 4.5 nm nanoparticles in hexane solution $\{[(Ag)_n] = 4 \times 10^{-3}$ M$\}$, large aggregates, 200 μm high and 100 μm large, are observed by scattering electron microscopy (Fig. 15A). Fig. 15A shows the presence of smaller aggregates surrounding the larger one. Furthermore, layers at the bottom of the aggregate are observed. To make sure that these aggregates are made of silver nanoparticles, EDX analyses were performed on the top of the aggregate and on the bottom (in the layer region). The analysis is made on a 0.786 $\mu m^3$ volume. The top of the aggregate consists of silver, carbon and sulfur atoms. This is fully consistent with a crystal made of silver nanosized particles coated by dodecanethiol. Analysis of the layers observed on the surrounding of the aggregate reveals mainly the presence of carbon atoms, due to cleaved graphite, and traces of silver atoms. This confirms the presence of mono- and multi-layers of silver nanosized particles observed by TEM.

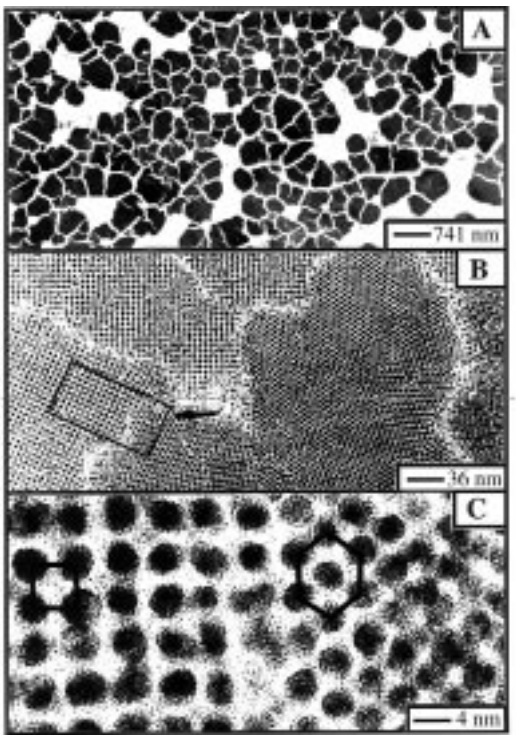


**Fig. 14** TEM micrographs of the grid at high magnification showing the different orientations of the silver particles. (A) General view, (B) and (C) various magnifications

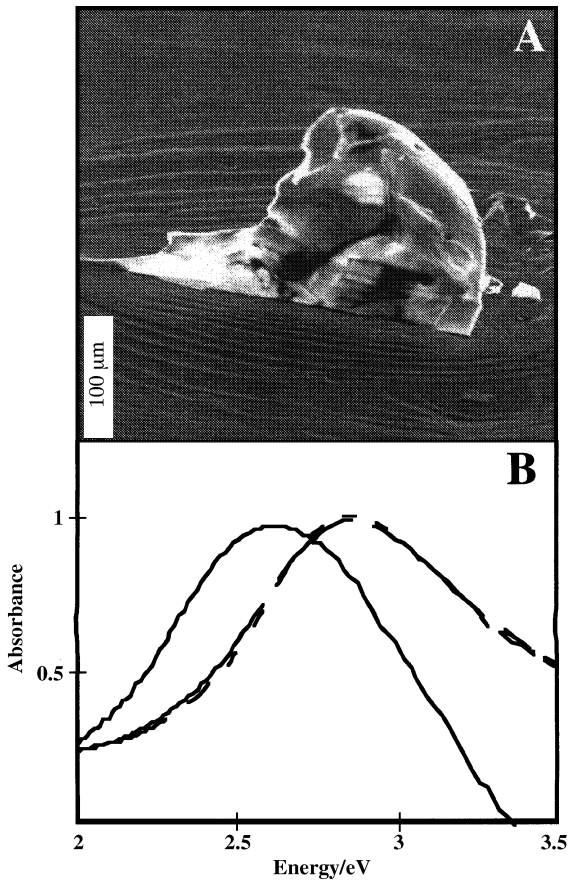


**Fig. 15** Silver nanoparticles of 4.5 nm average diameter. (A) Organized in fcc superlattices on a carbon support. (B) Absorption spectra of $(Ag)_n$ nanoparticles dispersed in solution (– – –) or arranged in a 3D superlattice (——)

The UV/VIS spectrum (Fig. 15B) of these aggregates shows a 0.25 eV shift toward lower energy of the plasmon peak with a slight decrease in the bandwidth (0.8 eV) compared to that observed in solution (0.9 eV). As observed above with the monolayer, by washing the support, the particles are redispersed in hexane and the absorption spectrum remains similar to that of the colloidal solution used to make the self-assemblies. The increase in the dielectric constant includes a shift to lower energy and an increase in the bandwidth of the plasmon peak.[34] For particles organized in an fcc structure, each silver nanoparticle is surrounded by 12 other clusters, whereas in a monolayer it has six neighbors. So in 3D superlattices, the dielectric constant surrounding each silver particle increases, inducing a larger plasmon peak shifted toward lower energy. This is confirmed when Fig. 13B and 15B are compared: the shift of the plasmon peak of particles arranged in 2D and 3D superlattices compared with the spectrum corresponding to free coated particles in hexane is 0.12 and 0.25 eV, respectively. According to the simulation and the data obtained above, the increase in the dielectric constant induces an increase in the plasmon peak bandwidth. This is not observed in Fig. 15B. The bandwidth is 0.8 eV, whereas for particles organized in a 2D superlattice (Fig. 13B) it is 1.3 eV. The value obtained for a 3D superlattice (0.8 eV) is close to that observed for free nanoparticles in hexane (0.9 eV). To explain such behavior, we have to take into account that, for a

given dielectric constant, the increase in the mean free path of the conduction electrons induces a decrease in the plasmon peak bandwidth. From this, it can be concluded that formation of 3D superlattices induces an increase in the free path of the conduction electrons. This is rather surprising, because the average distance between silver nanoparticles is 2 nm and we would not expect an electron tunneling effect through such a large barrier. However, a recent paper published by Ung *et al.*[54] claims that a 1–2 nm distance between two metal surfaces is small enough to allow tunneling of electrons across the double layers. Because we keep the same absorption spectrum and TEM pattern after washing the support, fusion between particles during the coverage can be excluded. Hence a collective effect, attributed to transport of the conduction electrons through the barrier due to the coating, takes place.

### II–VI semiconductor semimagnetic quantum dots, $Cd_{1-y}Mn_yS$

By using reverse micelles we have demonstrated, for $Cd_{1-y}Zn_yS$[16] and $Cd_{1-y}Mn_yS$,[17,55] that it is possible to control size and composition independently.[16]

When the $Cd_{1-y}Mn_yS$ syntheses are performed at various water contents and for a fixed composition, $y$, an increase in the particle size is observed. A red-shift in the absorption spectra when the particle size increases (Fig. 16) is also observed. Syntheses at a fixed water content and various compositions induce formation of particles having the same size and different compositions. Fig. 17 shows the change in the absorption spectrum with composition (the average diameter of the particles is 3 nm). The band gap energy, derived from the absorption spectra, depends on composition and particle size (Fig. 18). (*i*) For a given composition $y$, it increases with decreasing particle size. This phenomenon is attributed to a quantum size effect.[56] (*ii*) It decreases and then increases with increasing $y$ (Fig. 18). The band gap energy variation with composition is more pronounced when the particle size decreases and the position of its minimum depends on the particle size. For particles having an average diameter of 2 and 3.2 nm, this minimum is reached at $y$ equal to 0.05 and 0.08, respectively. Similar behavior is obtained in the bulk phase[40] and films.[57] The variation of the band gap energy with composition, $y$, is not very pronounced and does not have a well-defined minimum (about $y = 0.02$ to 0.05). These large changes in the behavior of the band gap energy with the size of nanoparticles and with the bulk phase could be attributed to perturbations induced by hybridization of magnetic cation orbitals ($Mn^{2+}$) with the band structure and to exchange interactions in a confined regime.[55]

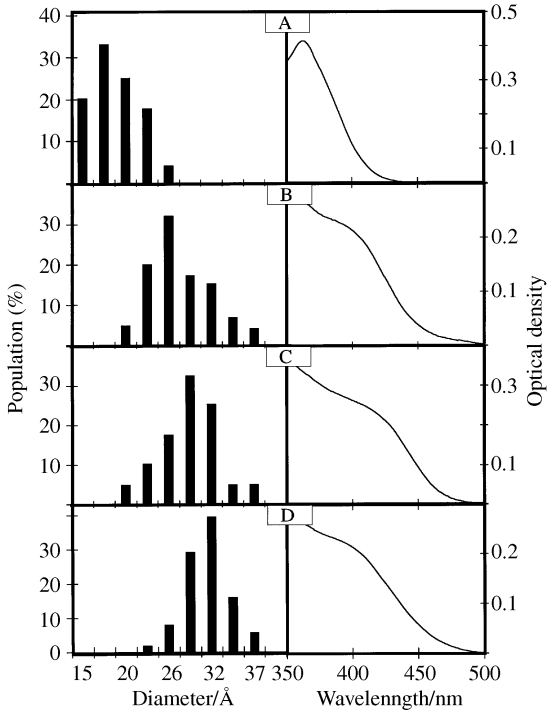


**Fig. 16** Population histograms derived from TEM patterns and absorption spectra of $Cd_{0.9}Mn_{0.1}S$ particles synthesized at various water contents $w$: (A) 5, (B) 20, (C) 30 and (D) 40

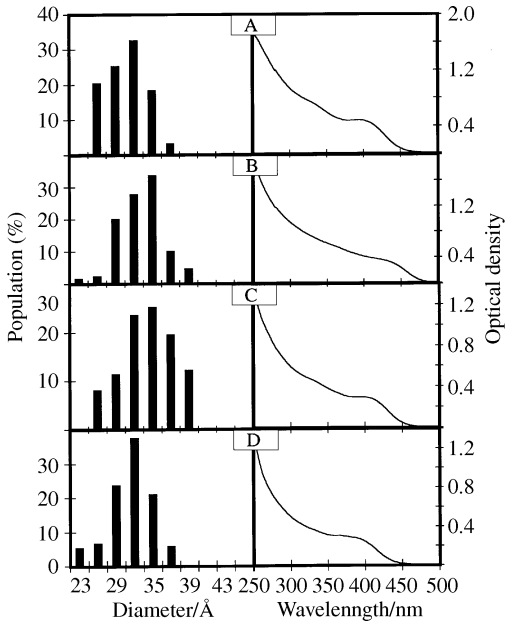


**Fig. 17** Population histograms deduced from TEM patterns and absorption spectra of $Cd_{1-y}Mn_yS$ particles at various $y$: (A) 0, (B) 0.08, (C) 0.12 and (D) 0.23. The size of the particles is kept constant at 3 nm

With the preparation mode, no changes in the energy band gap variation with composition and size are observed. In contrast, the fluorescence strongly differs with the aging of particles. To demonstrate this we prepared particles having the same average size and composition ($y = 0.05$) but differing by their aging. Particles **I** were synthesized at $w = 40$ ($w = [H_2O]/[AOT]$, see above) and dodecanethiol was immediately added to the micellar solution. A well-known selective surface reaction between the thio derivative and cations occurs. The coated nanocrystallites are extracted from the micelles, washed with ethanol and then dispersed in a mixture of two solvents (isopentane–methylcyclohexane (3 : 1), v : v) forming an optically clear glass at low temperature. Particles **II** were synthesized at $w = 10$ and kept in micellar solution. After 90 min dodecanethiol was added and the particles were immediately extracted from the micelles. The average diameter of particles **I** and **II** is 3.2 and 2.8 nm with a standard deviation of 10% and 16%, respectively. The composition, $y$,

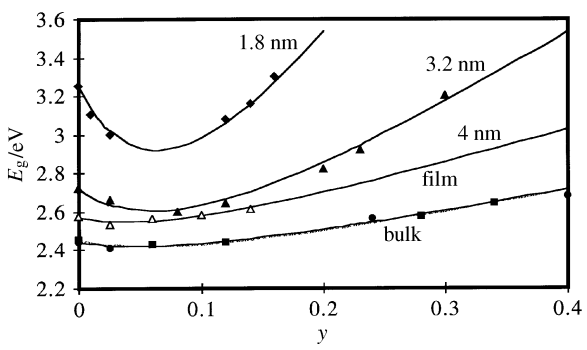


**Fig. 18** Band gap energy ($E_g$) of $Cd_{1-y}Mn_yS$ crystallites *vs.* manganese composition $y$ for different particle sizes. The bulk curve values are taken from ref. 58

determined by energy dispersion spectroscopy is 0.05. As described in our previous paper,[17] the EPR spectra of powders made of nanoparticles show that $Mn^{2+}$ ions are included in the CdS matrix. The nanocrystal structure, determined from electron diffraction, is zinc blende.

Photoluminescence (PL) spectra of particles **I** and **II** are compared at room temperature (Fig. 19A and C) and 77 K (Fig. 19B and D) with 400 nm excitation wavelength. The PL spectrum of particles **I** shows, at room temperature, a large band with a maximum close to 700 nm. It is similar to that obtained without $Mn^{2+}$ ions included inside the CdS matrix and is attributed to CdS defect states[8,59] (Fig. 19A). As expected, the PL spectrum is more intense at 77 K and a slight blue-shift due to dilatation of the lattice with increasing temperature[60] is observed (Fig. 19B). Hence, PL spectra of particles **I** are characterized by CdS defect states and no luminescence due to isolated $Mn^{2+}$ ions is observed. This behavior differs markedly with particles **II**: at room temperature, the PL spectrum is broad with a maximum centered at 680 nm and a shoulder at 600 nm (Fig. 19C). The PL spectrum is fitted by assuming two Gaussian curves and two spectra are derived: the spectrum designated 1 in Fig. 19C is characterized by a maximum centered at 585 nm and is attributed to the PL spectrum of isolated $Mn^{2+}$ ions. The simulated halfwidth of the $Mn^{2+}$ luminescence is 0.23 eV, which is in good agreement with that determined for $Mn^{2+}$ luminescence in the bulk phase and in $Zn_{1-y}Mn_yS$ nanoclusters.[61–66] At 77 K, this behavior is reinforced: particles **I** show the CdS trap emission (Fig. 19B) whereas **II** presents a PL spectrum characterized by a maximum centered at 590 nm (Fig. 19D). As above, two subspectra are derived from the simulation: one centered at 585 nm, with a halfwidth of 0.23 eV (designated 1), and the other at 650 nm (designated 2). The PL spectrum due to CdS defects and shown on Fig. 19D (number 2) is slightly red-shifted compared to that obtained in Fig. 19B. This is because the average size of particles **I** is slightly smaller (3.2 nm) than particles **II** (2.8 nm), see inserts Fig. 1A and C.

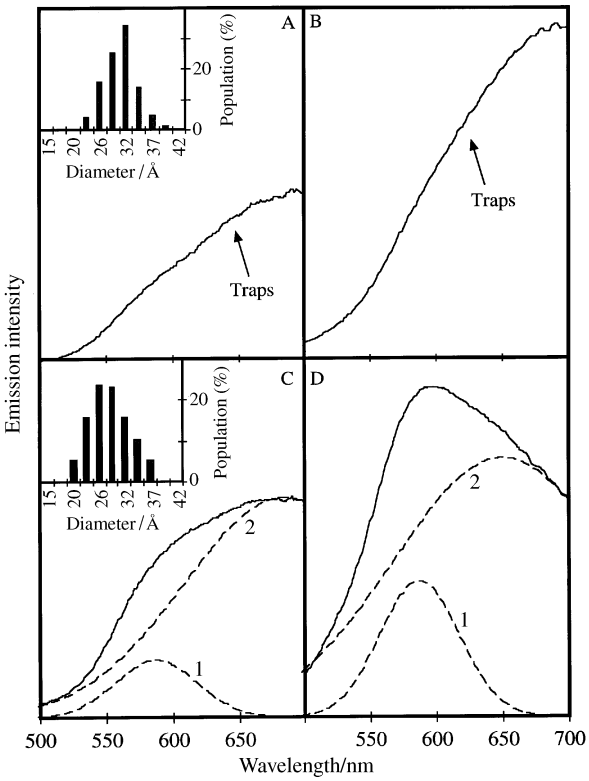


**Fig. 19** PL spectra of particles **I** (A, B) and **II** (C, D) recorded at room temperature (A, C) and at 77 K (B, D). Experimental (——) and simulated (– – –) spectra. See text for explanation of curves 1 and 2. Insert: Population histograms of particles **I** and **II** ($\lambda = 400$ nm)

Particles **III** and **IV**, characterized by 4.0 and 4.2 nm average diameters, were synthetized at $w$ equal to 40 and 10, respectively. For particles **III**, dodecanethiol was added immediately after synthesis and they were extracted from the micelles after 48 h. For particles **IV**, dodecanethiol was added 48 h after the synthesis and they were immediately extracted from the micelles. The PL spectrum of **III** at 250 K shows CdS trap emission. By decreasing the temperature, the fluorescence due to isolated $Mn^{2+}$ ions appears (Fig. 20A). With **IV** the PL spectrum (Fig. 20B), recorded at room temperature, shows a marked increase in the relative fluorescence due to isolated $Mn^{2+}$ ions compared to that due to CdS defects. Hence, the PL spectra of particles having similar sizes (4 and 4.2 nm) and differing in the aging mode differ markedly: particles aged for 48 h (**IV**) show isolated $Mn^{2+}$ fluorescence at room temperature, whereas it can only be observed with decreasing temperature for particles **III**. As described above, simulation of the PL spectra by two Gaussians shows one spectrum centered at 585 nm and another at longer wavelengths, attributed to CdS defect states. The relative areas of these PL spectra, recorded in wavenumbers, is obtained by integration. At room temperature, the ratio of the spectrum area due to isolated $Mn^{2+}$ ions relative to that due to the trap emission is 0, 0.09, 0.05 and 1 for particles **I**, **II**, **III** and **IV**, respectively. Hence, the relative luminescence intensity due to isolated $Mn^{2+}$ ions is size independent and varies with the aging of the particles.[65] This cannot be attributed to a change in the amount of $Mn^{2+}$ inside the CdS matrix for the following reasons. (*i*) The difference between $Cd_{0.95}Mn_{0.05}S$ and CdS band gap energies is quite similar for 3.2 and 2.8 nm nanoparticles. The slight variation is due to the difference in particle size. We know that the $Cd_{1-y}Mn_yS$ band gap changes markedly with composition. So, if $y$ had changed these differences would be much larger. (*ii*) From the EDS, the average composition is kept at 5%. (*iii*) $Mn^{2+}$ EPR spectra of a powder made of $Cd_{0.95}Mn_{0.05}S$ nanoparticles are observed. (*iv*) When particles are progressively annealed, the 585 nm luminescence intensity progressively decreases to reach zero at 200 °C. This decrease is correlated with the disappearance of $Mn^{2+}$ observed by EDS.

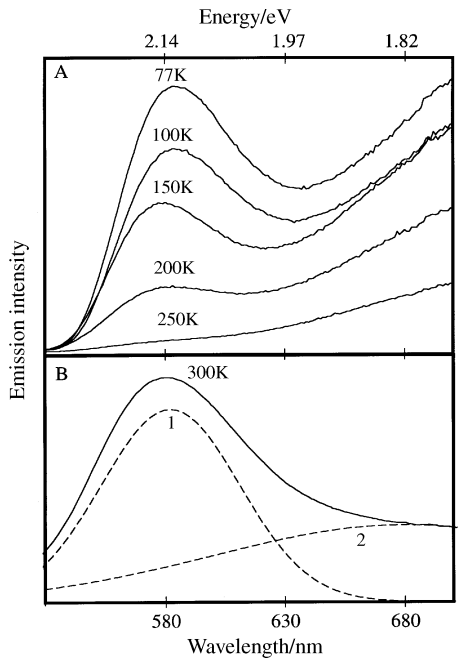


**Fig. 20** (A) Variation of the PL spectrum of particles **III** with temperature. (B) PL spectrum of particles IV at room temperature ($\lambda = 400$ nm). Experimental (——) and simulated (– – –) spectra. See text for explanation of curves 1 and 2

From these observations it can be concluded that the PL due to isolated $Mn^{2+}$ ions in $Cd_{0.95}Mn_{0.05}S$ nanoclusters made in reverse micelles is observed when the particles are aged. Apparently, these results markedly differ from those seen with $Zn_{1-y}Mn_yS$[63–65] and $Cd_{1-y}Mn_ySe$[66] nanocrystallites. A careful study of the published[63,64,66] experimental conditions clearly indicates that the luminescence due to isolated $Mn^{2+}$ ions in a semiconductor matrix was observed when the particles are aged and/or have been subjected to a thermal treatment. Hence, the $Mn^{2+}$ luminescence observed in nanoclusters, at room temperature, cannot be attributed to a quantum size effect, as has been claimed previously.

## Conclusion

It has been possible to determine the dependence of optical properties on size and shape of nanoparticles.

The size of metal particles such as silver and copper is controlled by using colloidal assemblies as templates. The size distribution is within a range of $\pm 10\%$ of the average. This confirms the prediction, from extended Mie theories, in which the plasmon peak progressively disappears when the particle size is comparable to the mean free path of the conduction electron. Again, as expected from theory, the change in the shape of the material induces a red-shift in the plasmon peak that depends on the size of the prolate particles. When particles are arranged in 2D and 3D superlattices, the optical properties strongly differ. In the latter case electron tunnelling through a barrier takes place.

For II–VI semiconductors, the colloidal method developed in our laboratory permits the size and composition to be controlled independently. In opposition to what has been claimed previously, the fluorescence of isolated $Mn^{2+}$ ions cannot be attributed to a quantum size effect but to the aging of the material.

## Acknowledgements

I would like to thank very much my coworkers who have been in charge of these studies. Special thanks are due to F. Billoudet, N. Feltin, D. Ingert, L. Levy, Dr. I. Lisiecki, Dr. C. Petit and A. Taleb, who did the work, and to A. Filakembo and S. Dider-Jean for technical assistance.

## References

1 M. P. Pileni, *J. Phys. Chem.*, 1993, **97**, 6961.
2 M. P. Pileni, *J. Phys. Chem.*, 1993, **97**, 6961.
3 I. Lisiecki and M. P. Pileni, *J. Am. Chem. Soc.*, 1993, **115**, 3887.
4 C. Petit, P. Lixon and M. P. Pileni, *J. Phys. Chem.*, 1993, **97**, 12974.
5 A. Wokaun, J. P. Gordon and P. F. Liao, *Phys. Rev. Lett.*, 1982, **48**, 957.
6 I. Lisiecki and M. P. Pileni, *J. Phys. Chem.*, 1995, **99**, 5077.
7 I. Lisiecki, M. Borjling, L. Motte, B. Ninham and M. P. Pileni, *Langmuir*, 1995, **11**, 2385.
8 L. E. Brus, *J. Chem. Phys.*, 1983, **79**, 5566.
9 R. Rossetti, J. L. Ellison, J. M. Bigson and L. E. Brus, *J. Chem. Phys.*, 1984 **80**, 4464.
10 C. Petit and M. P. Pileni, *J. Phys. Chem.*, 1988, **92**, 2282.
11 M. L. Stigerwald, A. P. Alivisatos, J. M. Gibson, T. D. Harris, R. Kortan and A. J. Muller, *J. Am. Chem. Soc.*, 1988, **110**, 3046.
12 C. Petit, P. Lixon and M. P. Pileni, *J. Phys. Chem.*, 1990, **94**, 1598.
13 B. H. Robinson, A. N. Khan-Lodhi and T. F. Towey, *J. Chem. Soc., Faraday Trans.*, 1990, **86**, 3757.
14 L. Motte, C. Petit, P. Lixon, L. Boulanger and M. P. Pileni, *Langmuir*, 1992, **8**, 1049.
15 T. Hirai, H. Sato and I. Komasawa, *Ind. Eng. Chem. Res.*, 1994, **33**, 3262.
16 J. Cizeron and M. P. Pileni, *J. Phys. Chem.*, 1995, **99**, 17410.
17 L. Levy, J. F. Hochepied and M. P. Pileni, *J. Phys. Chem.*, 1996, **100**, 18322.
18 For example, see the special issue on Nanostructured Materials, *Chem. Mater.*, 1996, **8**, 5.
19 A. E. Hughes and S. C. Jain, *Adv. Phys.*, 1979, **20**, 717 and references therein.
20 U. Kreibig, C. V. Fragstein, *Z. Phys.*, 1962, **224**, 307.
21 M. Meier and A. Wokaun, *Opt. Lett.*, 1983, **8**, 581.
22 C. C. Lam, P. T. Leung and K. Young, *J. Opt. Soc. Am. B*, 1992, **9**, 1585.
23 L. Genzel, T. P. Martin and U. Kreibig, *Z. Phys. B*, 1975, **21**, 339.
24 *Absorption and Scattering of Light by Small particles*, eds. C. F. Bohren and D. R. Huffman, Wiley, New York, 1983.
25 S. Mochizuki and R. Ruppin, *J. Phys.: Condens. Matter*, 1993, **5**, 135.
26 K. P. Charlé and W. Schulze, *Ber. Bunsenges. Phys. Chem.*, 1984, **88**, 350.
27 G. Mie, *Ann. Phys.*, 1908, **25**, 377.
28 J. A. Greighton and D. G. Eaton, *J. Chem. Soc., Faraday Trans. 2*, 1991, **87**, 3881.
29 C. V. Fragstein and H. Roemer, *Z. Phys.*, 1958, **151**, 54.
30 H. Roemer and C. V. Fragstein, *Z. Phys.*, 1961, **163**, 27.
31 C. V. Fragstein and F. J. Schoenes, *Z. Phys.*, 1967, **198**, 477.
32 H. Fröhlich, *Elektronentheorie der Metalle*, Springer, Berlin, 1936.
33 E. J. Zeman and G. C. Schatz, *J. Phys. Chem.*, 1987, **91**, 634.
34 M. P. Cline, P. W. Barber and R. K. Chang, *J. Opt. Soc. Am. B*, 1986, **3**, 15.
35 D. S. Wang and M. Kerber, *Phys. Rev. B*, 1981, **24**, 1777.
36 J. I. Gersten and A. Nitzan, in *Surface Enhanced Raman Scattering*, ed. R. K. Chang and T. E. Furtak, Plenum Press, New York, 1982, p. 89.
37 *Reactivity in Reverse Micelles*, ed. M. P. Pileni, Elsevier, Amsterdam, 1989.
38 T. F. Towey, A. Khan-Lodl and B. H. Robinson, *J. Chem. Soc., Faraday Trans. 2*, 1990, **86**, 3757.
39 C. Robertus, J. G. H. Joosten and Y. K. Levine, *J. Chem. Phys.*, 1990, **93**, 7293.
40 G. Cassin, J. P. Badiali and M. P. Pileni, *J. Phys. Chem.*, 1995, **99**, 12941.
41 T. K. Jain, G. Cassin, J. P. Badiali and M. P. Pileni, *Langmuir*, 1996, **2**, 2408.
42 Y. Moroi, K. Motomura and R. Matuura, *J. Colloid Interface Sci.*, 1974, **46**, 111.
43 C. Petit, T. K. Jain, F. Billoudet and M. P. Pileni, *Langmuir*, 1994, **10**, 4446.
44 A. Henglein and R. Taush-Treml, *Colloid Interface Sci.*, 1981, **80**, 84.
45 M. Mostafavi, N. Keghouche, M. O. Delcourt and J. Belloni, *Chem. Phys. Lett.*, 1990, **167**, 193.
46 K. C. Yi, Z. Horvolgyi and J. H. Fendler, *J. Phys. Chem.*, 1994, **98**, 3872.
47 C. D. Bain and G. M. Whitesides, *J. Am. Chem. Soc.*, 1989, **111**, 7155.
48 U. Kreibig, *J. Phys. F: Metal. Phys.*, 1974, **4**, 999.
49 P. Mulvaney, T. Linnert and A. Henglein, *J. Phys. Chem.*, 1991, **95**, 7843.
50 A. Yanase and H. Komiyama, *Surf. Sci.*, **248**, 1991, 11.
51 I. Lisiecki, F. Billoudet and M. P. Pileni, *J. Phys. Chem.*, 1996, **100**, 4160.
52 A. Taleb, C. Petit and M. P. Pileni, *Chem. Mater.*, 1997, **9**, 950.
53 A. Taleb, C. Petit and M. P. Pileni, *J. Phys. Chem.*, in press.
54 T. Ung, M. Giersig, D. Dunstan and P. Mulvaney, *Langmuir*, 1997, **13**, 1773.
55 L. Levy, N. Feltin, D. Ingert and M. P. Pileni, *J. Phys. Chem.*, 1997, **101**, 9153.
56 A. J. Nozik, F. Williams, M. T. Nenadocic, T. Rajh and O. I. Micic, *J. Phys. Chem.*, 1985, **89**, 397.
57 C. T. Tsai, S. H. Chen, D. S. Chuu and W. C. Chou, *Phys. Rev. B*, 1996, **54**, 11555.
58 M. Ikeda, K. Itoh and S. Hisano, *J. Phys. Soc. Jpn.*, 1968, **25**, 455.
59 J. L. Coffer, S. R. Bigham, R. F. Pinizzotto and H. Yang, *Nanotechnology*, 1992, **3**, 69.
60 Y. P. Varshni, *Physica*, 1967, **34**, 149.
61 R. N. Bhargava, *J. Lumin.*, 1996, **70**, 85.
62 R. N. Bhargava, D. Gallagher, X. Hong and A. Nurmikko, *Phys. Rev. Lett.*, 1994, **72**, 416.
63 Y. Wang, N. Herron, K. Moller and T. Bein, *Solid State Comm.*, 1991, **77**, 33.
64 R. N. Bhargava, D. Gallagher and T. Welker, *J. Lumin.*, 1994, **60/61**, 275.
65 L. Levy, D. Ingert and N. Feltin, *Adv. Mater.*, 1997, in press.
66 Y. Oka and K. Yanata, *J. Lumin.*, 1996, **70**, 35.

*Received in Montpellier, France, 19th September* 1997;
*Paper* 7/09218K